Systematic study of magnetic linear dichroism and birefringence in (Ga,Mn)As

N. Tesařová,[1] T. Ostatnický,[1] V. Novák,[2] K. Olejník,[2] J. Šubrt,[1] H. Reichlová,[2,1] C. T. Ellis,[3] A. Mukherjee,[3] J. Lee,[3] G. M. Sipahi,[4,3] J. Sinova,[5,2] J. Hamrle,[6] T. Jungwirth,[2,7] P. Němec,[1] J. Černe,[3] and K. Výborný[2,3]

[1]*Faculty of Mathematics and Physics, Charles University in Prague, Praha, CZ-121 16, Czech Republic*

[2]*Institute of Physics, ASCR, v. v. i., Cukrovarnická 10, CZ-16253 Praha 6, Czech Republic*

[3]*Department of Physics, University at Buffalo–SUNY, Buffalo, New York 14260, USA*

[4]*Instituto de Física de São Carlos, Universidade de São Paulo, CP 369, 13560-970, São Carlos, SP, Brazil*

[5]*Department of Physics, Texas A&M University, College Station, Texas 77843-4242, USA*

[6]*Department of Physics and Nanotechnology Centre, Technical University of Ostrava, 17. listopadu 15, CZ-70833 Ostrava-Poruba, Czech Republic*

[7]*School of Physics and Astronomy, University of Nottingham, Nottingham NG7 2RD, United Kingdom*

(Received 26 August 2013; revised manuscript received 12 December 2013; published 14 February 2014)

Magnetic linear dichroism and birefringence in (Ga,Mn)As epitaxial layers is investigated by measuring the polarization plane rotation of reflected linearly polarized light when magnetization lies in the plane of the sample. We report on the spectral dependence of the rotation and ellipticity angles in a broad energy range of 0.12–2.7 eV for a series of optimized samples covering a wide range on Mn dopings and Curie temperatures and find a clear blueshift of the dominant peak at energy exceeding the host material band gap. These results are discussed within the framework of the $k \cdot p$ and mean-field kinetic-exchange model of the (Ga,Mn)As band structure. We infer that disorder-induced nondirect transitions significantly influence magneto-optical properties of (Ga,Mn)As.

DOI: 10.1103/PhysRevB.89.085203 PACS number(s): 75.47.−m

I. INTRODUCTION

Among optical spectroscopies, differential methods based on the birefringence or the dichroism, i.e., sensitive to differences in refractive indices between two optical modes, can give more information on material electronic structure than absorption measurements [1]. For instance, the absorption coefficient $\alpha(\omega)$ in the dilute magnetic semiconductor (DMS) [2] (Ga,Mn)As is essentially featureless [3] at frequencies ω close to $E_g/\hbar$ (the band-gap energy, $E_g \approx 1.52$ eV for GaAs) while the same material in the same frequency range exhibits a strong peak in polarization plane rotation caused by the magnetic linear dichroism and birefringence [4]. At the same time, any type of magnetism-induced dichroism or birefringence depends on the ferromagnetic splitting of the bands (related to saturated magnetization $\vec{M}$) and manganese-doped DMSs like (Ga,Mn)As offer the unique possibility of tuning the strength of magnetism by varying the Mn content x_{nom} over a broad range. Studying the trends in magneto-optical spectra across a series of samples with increasing Mn doping and comparing them to model calculations allows one to microscopically relate the individual spectral features to the electronic structure of the (Ga,Mn)As material.

Polarization-resolved magneto-optical effects appear in a multitude of geometries and setups which we review in more detail in Sec. II below. In terms of the leading order of the effect, they can be divided into effects linear and quadratic in $\vec{M}$. In both cases, an incident light beam linearly polarized along $\hat{x}'$ turns into an elliptically polarized one whose major axis is rotated with respect to $\hat{x}'$ by an angle θ. The degree of ellipticity is characterized by another (typically also small) angle ψ. Both angles are defined in Fig. 1(a). Effects linear (or more generally odd) in $\vec{M}$ give $\theta(-\vec{M}) = -\theta(\vec{M})$ and are related [5,6], for $\omega \to 0$, to the dc anomalous Hall effect [7]. These effects are more commonly investigated as they are often simpler to experimentally access. They are typically larger and it is simpler to separate them from magnetization-independent optical signals. On the other hand, even effects (quadratic in the leading order of $\vec{M}$) with $\theta(-\vec{M}) = \theta(\vec{M})$ appear in literature less frequently. For example, the Voigt effect in reflection (see Sec. II and Fig. 2) has first been reported as late as in 1990 [8]. Yet, they offer an alternative probe into the electronic structure of the material distinct from what is probed in odd-in-$\vec{M}$ measurements. The effects even in $\vec{M}$ are related to the anisotropic magnetoresistance (AMR) [9,10] for $\omega \to 0$ and they do not vanish in certain situations where the effects odd in $\vec{M}$ do. For example, in compensated antiferromagnets, the magneto-optical effects even in $\vec{M}$ can still be detected [11] because contributions from the two spin sublattices with opposite spin orientations do not cancel. As a probe into the antiferromagnetic order [12], magneto-optical effects in the visible and infrared range, such as the one described in this paper, do not require large-scale facilities as the measurements of neutron diffraction [13] or x-ray Voigt effect [14] do.

The magneto-optical effects odd in $\vec{M}$ have been extensively explored in (Ga,Mn)As [2,6,15,16]. While the visible [15,16] range provides information on transitions between valence and conduction bands which are relatively less sensitive to the spin-orbit interaction effects, infrared [6] spectra enable us to explore transitions within valence bands. Quadratic (even in $\vec{M}$) magneto-optical response of (Ga,Mn)As is an alternative probe into its electronic structure. In analogy with the dc anisotropic magnetoresistance, it crucially depends on the spin-orbit interaction in the whole spectral range. Previous experiments have focused on measurements of the even in $\vec{M}$ magneto-optical effects in selected (Ga,Mn)As samples without studying their spectral dependence [17] or limiting themselves to the visible spectral range [4,18], Here, we report measurements in a spectral range of 0.12–2.7 eV and study systematically the magneto-optical spectra even in $\vec{M}$ across a series of optimized (Ga,Mn)As materials

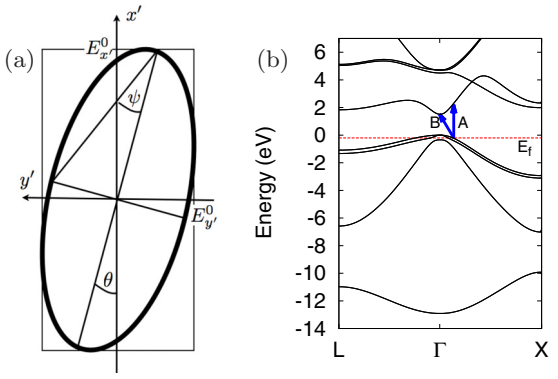

FIG. 1. (Color online) (a) Measured magneto-optical quantities. Originally linearly polarized beam becomes elliptically polarized after interaction with the sample. Its ellipticity is characterized by angle ψ and the rotation of the major axis is θ. (b) GaAs host band structure with Fermi level E_f typical for our Mn-doped samples. Arrows indicate direct (A) and nondirect (B) transitions from the Fermi surface to the conduction band.

spanning a broad Mn-doping range summarized in Table I below.

Section II is dedicated to a brief overview of magneto-optical effects and clarification of the terminology that is not coherent across the literature [1,4]. Our experimental data are presented in Sec. III and we compare them in Sec. IV to a kinetic-exchange model [19] based calculation of ac permittivity that allows us to determine $\theta(\omega)$ and $\psi(\omega)$. In

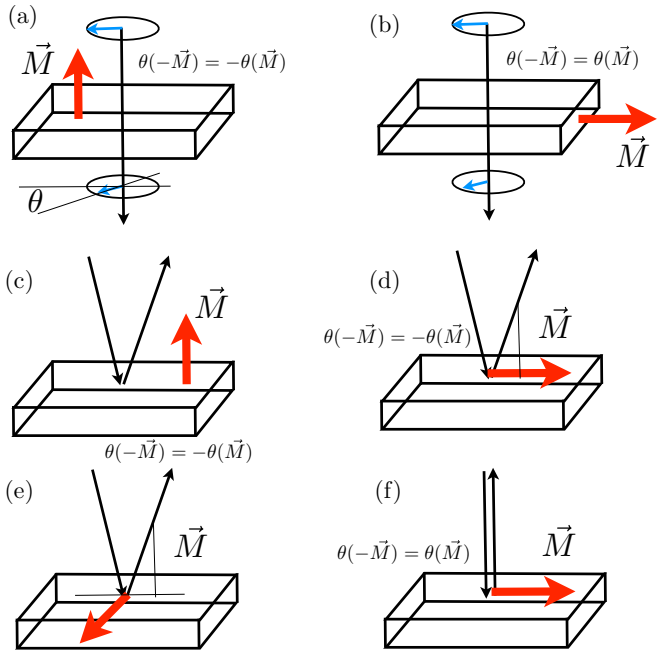

FIG. 2. (Color online) Selected magneto-optical effects. Polarization planes of incoming and outgoing beams are rotated by θ with respect to each other (possible ellipticity ψ of the outgoing is not considered in these sketches). (a) Faraday effect, (b) Voigt effect, (c) polar Kerr effect (or simply Kerr effect in the limit of normal incidence), (d) longitudinal Kerr effect, (e) transversal Kerr effect, (f) Voigt effect in reflection.

TABLE I. Basic sample parameters according to Table I of [16] (Supplemental Information). Asterisk indicates estimated value. Effective doping x [which enters Eq. (3) through the ferromagnetic splitting] is calculated from the measured saturated magnetization as explained in Appendix B.

	Wafer	x_{nom} (%)	x (%)	$10^{-21} \cdot p$ (cm^{-3})	T_c (K)
A	F010	1.5	1.0	0.15	29
B	F002	3	1.8	0.66	77
C	F020	5.2	3.6	1.08	132
D	E115	7	5.5	1.41	159
E	E122	9	6.9	1.55	179
F	E079	12.5	8.6	1.8*	186
G	F056	14	8.5	1.8*	182

Sec. IV, we also discuss the complex individual spectral features of $\theta(\omega)$ and clarify the role of linear birefringence and dichroism (see also Appendix C). Section V concludes the paper. In Appendix A, we review theoretical description of magneto-optical effects on the level of Maxwell's equations to which the permittivity tensor is the input. Appendixes B and C, respectively, contain more details on the transport calculation using the kinetic-exchange model, and details on the optical part modeling, e.g., multiple reflections on the (Ga,Mn)As epilayer.

II. OVERVIEW OF MAGNETO-OPTICAL EFFECTS

The purpose of this section is to recapitulate selected magneto-optical effects, clarify the terminology, and specify which of these effects is considered in this paper. The first magneto-optical phenomenon was observed by Michael Faraday in 1846, followed by another one found by John Kerr in 1877. They found that linearly polarized light transmitted through (Faraday's discovery) or reflected from (Kerr's discovery) a nonmagnetic material subject to magnetic field $\vec{B}$ has its polarization plane rotated. In their experiments, the wave vector of the propagating light $\vec{k}$ was parallel to $\vec{B}$. In 1899, Woldemar Voigt observed optical anisotropy of a nonmagnetic crystal for $\vec{k} \perp \vec{B}$ which can also cause similar rotation of the polarization plane. Historical overview of these and related discoveries can be found in the introductory parts of [1,20]. As a matter of definition, we will not include polarization-unrelated (or unresolved) effects such as cyclotron resonance into our further discussion [21].

Analogous phenomena are found in magnetic materials where, phenomenologically, $\vec{M}$ plays the same role as $\vec{B}$ in the original observations of Faraday, Kerr, and Voigt. Typical experiments involve a slab or thin layer of the material and, for simplicity, let us assume for now that it is not placed on a substrate and also that $\vec{k}$ is perpendicular to the plane of the sample surface ("normal incidence"). Faraday and Kerr magneto-optical effects arise for $\vec{M} \parallel \vec{k}$, i.e., out-of-plane magnetization, while Voigt effect occurs for in-plane magnetization ($\vec{M} \perp \vec{k}$). As has already been described above [see Fig. 1(a)], the incident beam is linearly polarized and the Kerr (Faraday or Voigt) effect is manifested in the rotation θ of the reflected (transmitted) beam polarization plane.

Any of these effects will, in general, be accompanied by a nonzero ellipticity characterized by ψ and both angles are sometimes combined into one complex quantity, e.g., the complex Faraday angle θ_F in [5]. The Voigt effect is even in $\vec{M}$ while the Faraday and Kerr effects are odd in $\vec{M}$. There is no broadly accepted term for the quadratic (even-in-$\vec{M}$) magneto-optical effect in the reflection at normal incidence with in-plane $\vec{M}$, although sometimes it is called quadratic magneto-optical Kerr effect (QMOKE) [23], Hubert-Schäfer effect [24], orientational magneto-optical effect [28,29], or it is included in the "reflection analogy to the Voigt effect" [30]. We will adopt here the last terminology. A schematic summary of the Faraday, Voigt, and Kerr effects and of the Voigt effect in reflection is shown in Fig. 2.

For other than the normal incidence, the odd-in-$\vec{M}$ magneto-optical effect in reflection splits up into three types. The conditions $\vec{M} \parallel \vec{k}$ and $\vec{M}$ perpendicular to the sample are now no longer characteristic of the Kerr effect. Rather, $\vec{M}$ can now be decomposed into out-of-plane component $M_\perp$ and in-plane components M_L (M_T) parallel (perpendicular) to the plane of incidence. The polar Kerr effect, sometimes also called magneto-optical Kerr effect (MOKE), is in the leading order linear in $M_\perp$ and it is the only effect odd in $\vec{M}$ that does not vanish for $M_L = M_T = 0$. The longitudinal and transversal Kerr effects depend on the in-plane components of magnetization and to separate them from the Voigt effect in reflection, the polarization signal dependence on the angle β between $\vec{M}$ and the polarization plane can be used. Unlike all three Kerr effects, the Voigt effect in reflection is proportional [30] to a combination of M_T^2, M_L^2, and $M_L M_T$ which, at normal incidence, combine into a $\sin 2\beta$ dependence.

On microscopical level, the Kerr and Voigt effects turn out to have very different origin. While both ultimately stem from the interplay of spin-orbit interaction and ferromagnetic splitting of the band structure, they depend on different components of the ac conductivity tensor. Focusing on the effects in transmission rather than reflection for simplicity, we explain in Appendix A that the rotation angle is

$$\theta \approx \frac{d\omega}{c} \frac{\mathrm{Im}\, \varepsilon_{xy}}{n_0} \tag{1}$$

for $\vec{M}$ perpendicular to the sample layer while it is

$$\theta \approx \frac{d\omega}{c} n_0 \mathrm{Re} \left(\varepsilon_{xx} - \varepsilon_{yy} - \frac{\varepsilon_{yz}^2}{\varepsilon_{zz}} \right) \tag{2}$$

for $\vec{M}$ in the sample plane where it breaks the axial symmetry. Similar to Eq. (1), the Kerr effect probes the off-diagonal component of the conductivity and it is therefore linked to the anomalous Hall effect. On the other hand, the Voigt effect in reflection probes the difference in diagonal components of the conductivity tensor which would, in the dc limit, correspond to AMR.

Due to the broken axial symmetry in the case of in-plane $\vec{M}$, selection rules for band-to-band optical transitions based on conservation of angular momentum are relaxed and the Voigt effects can provide additional information about the system compared to the polar Kerr effect. As with other magneto-optical phenomena, this effect includes rotation and ellipticity measured in the beam after its interaction with the sample and from now on, we associate the terms "rotation" (θ) and "ellipticity" (ψ) only with the Voigt effect in reflection (unless explicitly stated otherwise). Both rotation and ellipticity are related to complex refractive indices $n_\parallel$ and $n_\perp$ of two modes (see detailed explanation in Appendix A) linearly polarized parallel and perpendicular to $\vec{M}$. Rotation θ is caused both by magnetic linear birefringence $\Delta\bar{n} \equiv \mathrm{Re}\,(n_\perp - n_\parallel) \neq 0$ (MLB) and magnetic linear dichroism $\Delta\bar{k} \equiv \mathrm{Im}\,(n_\perp - n_\parallel) \neq 0$ (MLD); an illustrative example is given in Appendix C. More generally (not just in context of magneto-optical effects), birefringence $\Delta\bar{n} \neq 0$ can manifest itself in the well-known double-image refraction (propagation of ordinary and extraordinary rays through a slab of icelandic calcite described first by Rasmus Bartholin in 1669) while dichroism [1] $\Delta\bar{k} \neq 0$ can effectively lead to mode filtering. Note that the term MLD is sometimes confusingly used [4] both for $\Delta\bar{k} \neq 0$ and the nonzero difference in reflection coefficients of the two linearly polarized modes. We now proceed to describe our experimental results of rotation and ellipticity of the Voigt effect in reflection on (Ga,Mn)As samples.

III. EXPERIMENT

The samples used in our measurement are (Ga,Mn)As layers prepared by optimized molecular-beam epitaxy growth and postgrowth annealing procedures [31] with various nominal Mn doping ranging from $x_{\mathrm{nom}} = 1.5\%$ to 14% and cut into 4.5×5-mm chips. The basic material characteristics of our samples are listed in Table I, additional information can be found in the main text and supplemental information of [16,31]. All samples were grown on a GaAs substrate, producing a compressive strain which favors an in-plane orientation of the easy axes (EAs). The competition of in-plane cubic and uniaxial anisotropies results in our (Ga,Mn)As films in two magnetic EAs tilted from the [100] and [010] crystal axes towards the $[1\bar{1}0]$ in-plane diagonal [32]. The tilt angle increases [31] with increasing Mn doping. The sample substrates were wedged (1°) to avoid spurious signals that might appear due to the multiple reflections from the back side of the substrate. In order to measure the rotation and ellipticity angles θ and ψ in a broad energy range we developed a sensitive experimental technique which is described in detail in [18]. We use a Xe lamp (0.33–2.7 eV) with a double prism CaF_2 monochromator and discrete spectral lines from CO_2 (115–133 meV) and CO (215–232 meV) lasers [33]. Measurements are done in the reflection geometry close to normal incidence (≈6° with respect to the sample normal) whereas we assume that the polarization plane rotation due to the longitudinal Kerr effect is negligible [34]. The samples are mounted on a custom-made rotating sample holder attached to the cold finger which is cooled down to 15 K. The holder enables a precise rotation of the sample, and thus of the magnetization with respect to the incident polarization using external magnetic field $\vec{B}$, which is applied along a fixed in-plane direction.

Prior to the actual measurement of θ and ψ, the samples are rotated so that one of the EAs is set parallel to $\vec{B}$. Subsequent application of a moderately strong magnetic field

($B \equiv |\vec{B}| = 0.6$ T) forces the magnetization to align with this EA. After the magnetization is oriented along the EA parallel to $\vec{B}$, the magnetic field is turned off and the sample is rotated 45° away from the field axis. The sample orientation is kept fixed subsequently, and it is not changed during the measurement of θ and ψ. The magneto-optical response of the sample is measured using the polarization modulation technique at base frequency $f = 50$ kHz, where the reflected beam passes through the photoelastic modulator (PEM) [37]. The optical axis of the PEM is oriented 45° with respect to the magnetic field axis and the detected signals at f and $2f$ are proportional to ellipticity (ψ) and rotation (θ) of the reflected light polarization, respectively [33,37]. In the first step of the measurement, the polarization of the incident light is set parallel with the magnetization orientation, so any nonzero signal detected at f or $2f$ is just background unrelated to magneto-optical properties of the sample. In the second step we apply $B \approx 0.6$ T which rotates the magnetization to $\beta = 45°$ relative to the incident beam polarization. In this situation, the polarization components parallel and perpendicular to magnetization experience different (complex) indices of refraction, maximizing the rotation and ellipticity signals magnitude. The $\sin 2\beta$ dependence of θ has been checked [see Fig. 3(d) in [18]]. By taking a difference of θ (or ψ) between the first and second step, we obtain the pure magneto-optical signal. This procedure removes all sources of dichroism and birefringence of the optical components in our setup which are unrelated to magnetism of the sample and it replaces the commonly used $[\theta(\vec{M}) - \theta(-\vec{M})]/2$ protocol for magneto-optical phenomena odd in magnetization such as the Kerr effect. We note that in order to obtain the correct sign and magnitude of θ and ψ, a calibration procedure [5] has to be performed. A detailed description of our experimental methods is given in [18]. We also point out that by comparing the magneto-optical signal $\theta(\vec{M})$ to $\theta(-\vec{M})$ as shown in Fig. 4(a) of that reference, we verified, for our samples, the assumption of smallness of the longitudinal Kerr effect which is odd in $\vec{M}$.

Measured θ and ψ for samples B, C, D, E, and G of Table I are displayed in Fig. 3, while the remaining two samples are studied only using a different technique described below. Both rotation and ellipticity reach typically values of several 0.1 mrad, show distinct spectral features in the studied range $\hbar\omega = 115$ meV–2.7 eV, and often change sign as a function of radiation frequency ω. Such values are about an order of magnitude smaller than the Kerr effect [6] but still large enough to use the Voigt effect in reflection as an efficient method to detect an in-plane component of the magnetization [38]. In agreement with Kimel *et al.* [4] who studied a single $x_{\text{nom}} = 2\%$ sample, we observe a peak in $\theta(\omega)$ exceeding 0.5 mrad whose sign and position (above $\hbar\omega = 1.5$ eV) is consistent with this earlier result. In the more general context of magnetic materials, values of $\theta \approx 0.5$ mrad reported in Heusler alloys [39] are quoted as [23] "record QMOKE values." We remark that Voigt effect was also measured in manganese-doped II–VI materials. Reference [4] claims that magneto-optical response even in $\vec{M}$ is "drastically enhanced" in (Ga,Mn)As compared to that of (Cd,Mn)Te [40]. While we do not directly contradict this conclusion we find the comparison less conclusive. Magneto-optical effects in a paramagnetic system such as (Cd,Mn)Te are not spontaneous

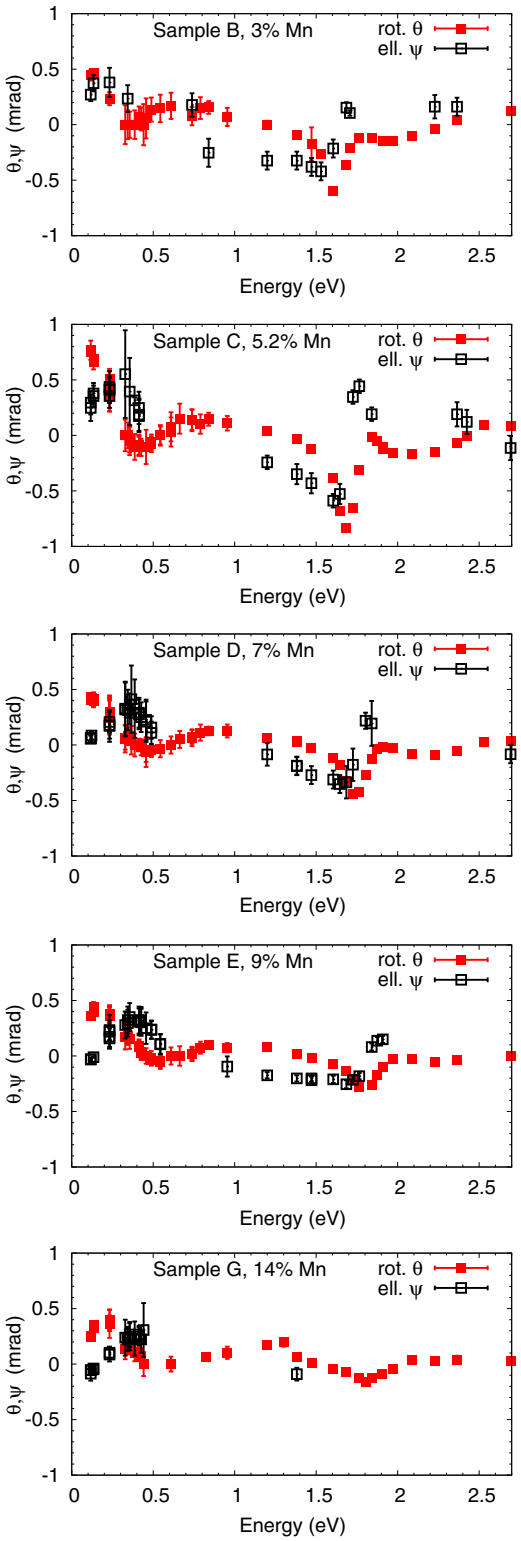

FIG. 3. (Color online) Measured spectral dependence of the rotation θ and ellipticity ψ for the Voigt effect in reflection. Manganese doping levels indicated correspond to x_{nom}.

but must be induced by external magnetic field, hence the spontaneous $\Delta\bar{n}$, $\Delta\bar{k}$ of (Ga,Mn)As must be compared to the proportionality constant between $\Delta\bar{n}$, $\Delta\bar{k}$ and B^2 in (Cd,Mn)Te, the so-called Verdet constant. More importantly

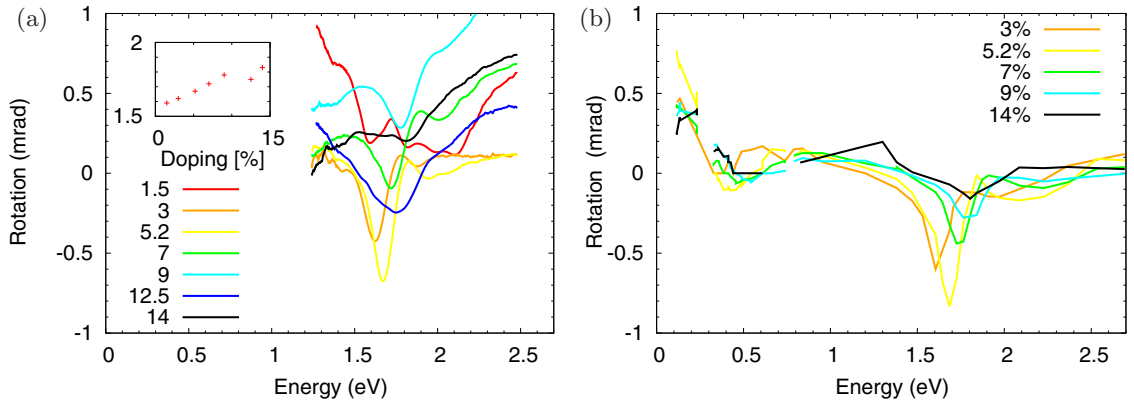

FIG. 4. (Color online) Overview of the measured rotation angle θ for samples A–G using (a) the subtraction of data above T_c and (b) the *in situ* rotation of $\vec{M}$. Inset in panel (a) shows the position in eV of the peak α as a function of Mn doping. All Mn concentrations indicated are x_{nom} (see Table I).

though, the transmission measurements [40] are limited to subgap frequencies where the signal is weaker and it is possible that the actual maximal magneto-optical response of (Cd,Mn)Te would be comparable to that of (Ga,Mn)As if we were comparing the parts of spectra that correspond to each other.

Another technique of removing the background unrelated to magnetism of the sample from the Voigt effect in reflection is to repeat the same measurement at low temperature and at $T > T_C$ and subtract the two. This technique is discussed in [18] and since the measured rotation at $T > T_C$ is typically larger than the pure signal from the sample [compare Fig. 3(b) in that reference], relatively large errors can be expected. This is confirmed by a comparison of the results of the two techniques in Fig. 4. Rotation angle spectra in panel (a) indeed exhibit vertical offsets of the order of 0.1 mrad between consecutive measurements as compared to data obtained by the method of magnetic-field-induced rotation of $\vec{M}$ summarized in panel (b). Even between two measurements of the same sample, $\theta(\omega)$ inferred by the former technique may be offset because of temperature dependence in optical properties of measurement setup elements. The peak at energies above 1.5 eV is nevertheless clearly seen using both methods and, even in the data of panel (a), its positions summarized in the inset systematically shift towards higher energies with increasing nominal doping of the samples. These positions agree very well with the data in panel (b) (see also Fig. 6). Note that panel (a) contains also data for samples A and F which were not measured using the more accurate technique.

The possibility to follow spectral trends as x_{nom} is varied is the main advance of our work as compared to previously published results [4]. We begin by noting that the prominent peaks in $\theta(\omega)$ above 1.5 eV shown in Fig. 4 appear close to the peaks of the Kerr effect [16], they shift to higher energies with increasing x_{nom} in both magneto-optical effects, and also the nonmonotonic dependence of their height on x_{nom} is similar. Going to smaller energies, there is a broad maximum followed by a relatively shallow minimum which also blueshifts from 300 meV (sample B) to 500 meV (sample G). At the lowest energies measured, $\theta(\omega)$ increases again and only in the sample with the highest doping is there a downturn around $\hbar\omega \approx$ 200 meV.

IV. INTERPRETATION OF THE MEASURED MAGNETO-OPTICAL SIGNALS

To understand observed spectral features in $\theta(\omega)$ and $\psi(\omega)$ of the Voigt effect in reflection and their trends across the set of samples, a model of the electronic bands close ($\sim\hbar\omega$) to the Fermi energy E_f is needed. Any model having ambitions to yield quantitative information on $\theta(\omega)$, $\psi(\omega)$ has to start from a description of the (Ga,Mn)As electronic structure reflecting the GaAs host bands, exchange splitting of the bands in the ferromagnetic state of (Ga,Mn)As, and the spin-orbit coupling. Without the last two components, only positions of spectral features in $\theta(\omega)$, $\psi(\omega)$ can be anticipated but not their shape and amplitude. The GaAs host band structure in Fig. 1(b), calculated by standard $spds^*$ tight-binding model [41], suggests that the prominent peak around 1.7 eV seen in $\theta(\omega)$ of Fig. 3 corresponds to transitions between valence and conduction band. To analyze its amplitude, we have to account for the combined effect of the exchange splitting and the spin-orbit interaction. Unlike other approaches such as the quantum defect method [42] used in [43] to analyze absorption spectra of (Ga,Mn)As, the kinetic-exchange model of disordered carrier bands [19,44], which we briefly describe below, naturally includes these two components. Apart from successfully explaining the spectral trends in absorption [45] and of the Kerr effect in the visible range [16], this model therefore allows us to calculate $\theta(\omega)$, $\psi(\omega)$ of the Voigt effect in reflection which is microscopically more constrained than the absorption or the visible range Kerr effect. We show below that results of this model reproduce the structure of the measured data as in the previously explored infrared Kerr effect [6] which also depends sensitively on the spin-orbit coupled exchange-split nature of the valence band.

The path to theoretically evaluated $\theta(\omega)$, $\psi(\omega)$ involves three steps, the first of which is to obtain the band structure $E_{\vec{k},a}$. Two of the aforementioned band-structure description components are included in $\hat{H}_{\mathrm{KL}}$ (host band structure and spin-orbit interaction), the last component (ferromagnetic exchange splitting) enters the total Hamiltonian through kinetic-exchange parametrized by J_{pd} (J_{sd}) couplings between the dominantly p-like valence band (s-like conduction band)

and Mn d levels:

$$\hat{H} = \hat{H}_{\mathrm{KL}} + \frac{J_{pd}}{\mu_B}\vec{M}\cdot\hat{s}_h + \frac{J_{sd}}{\mu_B}\vec{M}\cdot\hat{s}_e + \hat{V}_{xc}. \qquad (3)$$

Here, $\hat{s}_{e/h}$ is the electron/hole spin operator, μ_B is the Bohr magneton, and $\hat{V}_{xc}$ is the correction due to many-body and electrostatic effects. This correction, described in detail in Appendix B, accounts for the exchange energy between delocalized holes as well as their interaction with ionized dopant Mn atoms. The choice of bands included in the Kohn-Luttinger Hamiltonian $\hat{H}_{\mathrm{KL}}$ is dictated by the energy range ($\hbar\omega$ up to 2.7 eV) in our experiments and E_f of at most few 100 meV from the valence-band top. As seen in Fig. 1(b), only conduction band, heavy holes (HHs), light holes (LHs), and split-off band can be involved in optical excitations from occupied to unoccupied states making up the total number of eight bands in $\hat{H}_{\mathrm{KL}}$. Parameters entering this 8×8 matrix, including the relation between $\vec{M}$ and x, are given in Appendix B.

The second step is to calculate the conductivity tensor σ using the Kubo formula (see Appendix B) which can be recalculated into the permittivity tensor using

$$\varepsilon_{\mathrm{eff}} \equiv \varepsilon_0\left(\varepsilon_b + \frac{i\sigma}{\omega\varepsilon_0}\right). \qquad (4)$$

The value of ε_b is adjusted so that for intrinsic GaAs ($p = 0$), $\varepsilon_{\mathrm{eff}}$ calculated using Eq. (4) recovers the experimental ac permittivity at optical frequencies [46] and it approaches [47] $\varepsilon_\infty = 10.9$ for low $\hbar\omega$. For Voigt effect (in transmission), we would now use Eq. (2) to calculate the rotation angle θ and in our case, which is more complicated, we insert components of $\varepsilon_{\mathrm{eff}}$ of Eq. (4) into Eqs. (C1), (C2), (A6), and (A7) as described in Appendixes C and A. This last step involves classical optics describing the layered structure of our samples, including multiple reflections.

To address experimental findings in Fig. 3, we calculate $\theta(\omega)$ over a range of parameter values. Since ellipticity is experimentally somewhat more difficult to access [18], less data than for $\theta(\omega)$ are available and therefore we only briefly comment on $\psi(\omega)$ in the next paragraph. Given the span of p and x in Table I, we first show in Fig. 5 the calculated $\theta(\omega)$ for fixed $x = 5\%$ and varying p [panel (a)] and for fixed $p = 0.8\times 10^{21}$ cm^{-3} and varying x [panel (b)]. The order of magnitude of $\theta(\omega)$ and its structure (minimum-maximum-minimum for α-β-γ) agrees with experimental data in Fig. 3. Analyzing the contribution of individual terms in Eq. (B6), we confirm that peak α arises from optical transitions from the LH and HH bands to the conduction bands. Peaks β and γ are due to transitions within the valence bands. The intraband contribution to σ given by Eq. (B5) plays only a minor role and is noticeable only at the lowest energies considered here ($\hbar\omega \approx 100$ meV). A more detailed discussion of our model can be found in [48].

Our model of disordered valence band with kinetic-exchange splitting is known to give a qualitative and often semiquantitative description of various phenomena that originate in the spin-orbit coupled and ferromagnetically split electronic structure of (Ga,Mn)As [16]. Despite the utility of the model, its accuracy should not be overestimated. Rotation $\theta(\omega)$ and ellipticity $\psi(\omega)$ for parameters of sample E shown

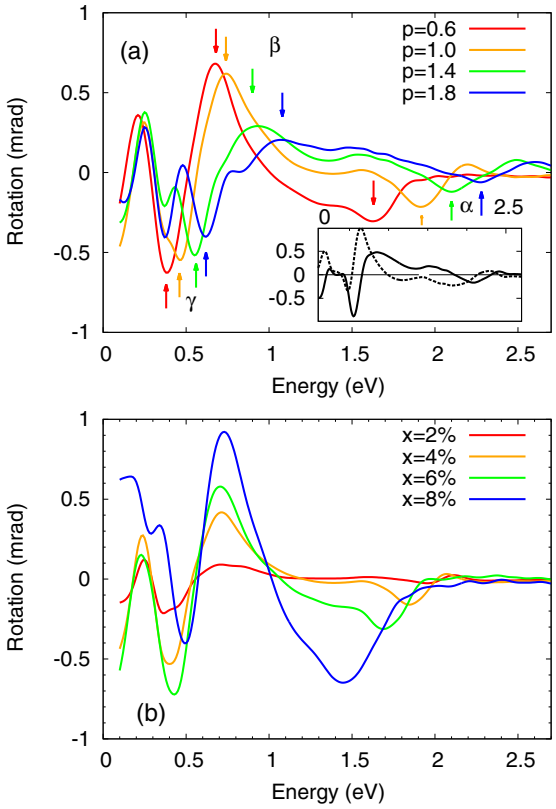

FIG. 5. (Color online) Calculated spectral dependence of the rotation angle θ for a series of systems with (a) $x = 5\%$ and varying p (in 10^{21} cm^{-3}) and (b) varying x and constant $p = 0.8\times 10^{21}$ cm^{-3}. Spectral features discussed in text are labeled by Greek letters. The inset shows rotation (solid) and ellipticity (dashed) for the parameters x and p corresponding to sample E.

in the inset of Fig. 5(a) do exhibit, in most cases, the same structure and order of magnitude as the experimental data in the top panel of Fig. 3 but there are some notable differences too. We first observe that peak α in $\theta(\omega)$ accompanied by the anti-Lorentzian structure in $\psi(\omega)$ in the inset appears at higher energies (2.09 eV) than in experiment (1.79 eV) and also that its magnitude is larger by a factor of 2 experimentally. We discuss the former observation later and focus on the peak magnitude first. The ac conductivity depends on the carrier scattering rate in a complicated way. In our approach, scattering enters our model via spectral broadening Γ in Eqs. (B5) and (B6) which is an approximation to the scattering rates that neglects their band dependence and anisotropy. We choose constant $\Gamma = 100$ meV, a value acceptable both from theoretical and experimental point of view. By tuning Γ or refining the scattering model (replacing it by $\Gamma^i_{kk'}$ which allowed us to successfully model the dc anisotropic magnetoresistance [49]), the agreement between model calculations and experiment could possibly be improved. Our model and experiments agree on the sign change of $\psi(\omega)$ at energies around 800 meV and also the position of the broad maximum β in $\theta(\omega)$ around 850 meV. The amplitude of calculated $\theta(\omega)$ is larger by a factor of 4 as compared to the experiment. Similarly, the minimum γ in $\theta(\omega)$ is much deeper in model calculations than in the experiment but their

positions (≈550 meV) agree well. As a consequence of this exaggerated feature, $\psi(\omega)$ exhibits a sign change and reaches a minimum around $\hbar\omega = 470$ meV because it is tied to $\theta(\omega)$ by the Kramers-Kronig relations. This minimum in $\psi(\omega)$ and also the downturn of $\theta(\omega)$ at the lowest observed energies ($\hbar\omega < 200$ meV) is not seen in experiments. We conclude that more theoretical work is needed to understand the Voigt effect at these low energies and return to higher energies where our model performs better.

We begin by analyzing the positions of peaks β and γ. Experimentally, the corresponding maximum and minimum in Fig. 3 are both found to blueshift with nominal doping of the samples. The broad maximum corresponding to peak β shifts from approximately 700 meV in sample B to about 1.0 eV in sample E and a similar, somewhat smaller, shift is found in model calculations. The calculated height of the maximum decreases as we go to samples with lower doping and approaches the experimental results within a factor of 2 for samples B and C. The blueshift of the minimum corresponding to peak γ when going from sample B to sample E also agrees well between model calculation (360 to 550 meV) and experiment (400 to 570 meV). As already mentioned, the model calculations strongly overestimate the depth of this minimum although at least the negative sign of $\theta(\omega)$ is observed in most samples. Next we focus on the position of peak α and discuss the main deficiency of our model, which we believe to be a very simplified account of disorder.

We extracted the position of peak α from the experimental data in Fig. 4 by fitting it to a Lorentzian. Data from panel (a) and (b) are shown as boxes and crosses in Fig. 6, respectively. The same procedure was repeated with our model calculations, where we took parameters x and p from Table I and used the calculated spectra $\theta(\omega)$. The corresponding peak positions are shown by the upper solid line in Fig. 6. Although the trend of shift towards higher energies is the same in the experiment and in the model, there is a clear difference of up to

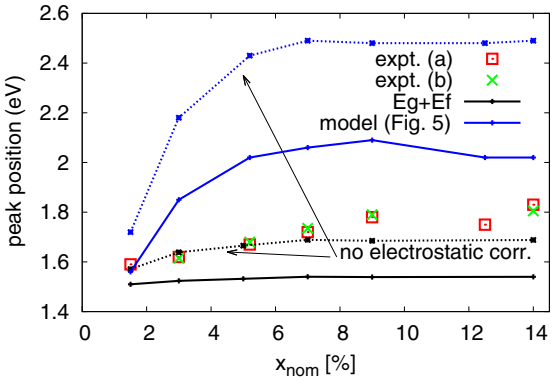

FIG. 6. (Color online) Positions of the α peak for the series of samples described by Table I. Experimental data (a) and (b) refer to Fig. 4. Model data (solid blue line) were extracted from calculations for x and p as given by Table I following the same procedure as those in Fig. 5. They take into account direct transitions only and the extreme limit of nondirect transitions (solid black) corresponds to $E_g + E_f$ where V_{xc} is also included. Dotted lines show these two limiting cases when electrostatic interaction with ionized acceptors is neglected.

300 meV, in other words, the blueshift is significantly slower in the experimental data. This is pointing to a shortcoming of our electronic-structure model represented by Eq. (3) where the presence of Mn is effectively treated in a mean-field virtual-crystal approximation. At the level of the Kubo formula in Eq. (B6), our model only allows for direct transitions and below we proceed to discuss how the experimental values of the peak α positions could possibly be explained by considering nondirect transitions.

Treating a realistic band structure and disorder on equal footing is a complicated task. Disorder broadening Γ which appears in the Kubo formula (B6) is only a poor approximation to the nonconservation of wave vector $\vec{k}$ in the strong-disorder case. Due to disorder in the crystal caused primarily by random positions of Mn atoms substituting for the cations of the host lattice, the Bloch theorem does not apply and $\vec{k}$ is not a good quantum number. Even in the extreme case of an amorphous continuous covalent network [50], the main features of electronic structure including the spin-orbit interaction remain preserved. One possible way of estimating the effect of disorder on optical transitions is therefore to lift the restriction of wave vector conservation while keeping the band structure otherwise unchanged [51] (i.e., neglecting the band gap reduction [52]). In terms of Fig. 1(b), this means considering transitions labeled "B" rather than only the direct transitions labeled "A." In terms of the Kubo formula (B6), this could approximately be implemented by replacing matrix elements $v_j^{ab\vec{k}\vec{k}'} \propto \delta_{\vec{k}\vec{k}'}$ by another function of $\vec{k},\vec{k}'$ (or even a constant). In the spirit of Moss-Burstein shift [53,54], the lowest-energy optical transition would then appear close to energy $E_f + E_g$ [see again panel (b) of Fig. 1] and we show this energy in Fig. 6 by the lower solid line. The experimental data lie approximately halfway between the two solid lines which suggests that disorder should be treated more carefully in our model than just by the simple spectral broadening in Eq. (B6). We also remark that the electrostatic interaction of holes with ionized Mn acceptors, included in $\hat{V}_{xc}$ of Eq. (3), significantly contributes to the position of peak α. The dotted lines in Fig. 6 show the model results when this factor is disregarded.

V. CONCLUSIONS

Rotation $\theta(\omega)$ and ellipticity $\psi(\omega)$ measured for the Voigt effect in reflection, a direct consequence of the magnetic linear dichroism and birefringence, represent a much more sensitive spectroscopic probe into the electronic structure of (Ga,Mn)As than, for instance, unpolarized optical-absorption experiments. Our measured data are compatible with the previously published $\theta(\omega)$ on selected samples and limited spectral range and we investigate variations of the spectra with manganese doping which influences both the exchange-splitting and Fermi level. We confirm that θ at energies exceeding the gap of the GaAs host can reach values larger than so far reported in other ferromagnetic materials. The corresponding peak is found to blueshift with increasing manganese doping and we analyze this trend using the $k \cdot p$ mean-field kinetic-exchange model. We find that even with exchange-correlation band renormalization effects taken into

account, this model yields appreciably larger energies at which this feature is seen, compared to experiment, and we attribute this fact to the neglected nondirect transitions caused by the disorder. Apart from this deficiency, the model correctly reproduces the structure of experimentally determined $\theta(\omega)$ ranging 112 meV–2.7 eV and $\psi(\omega)$ for energies above 500 meV. A more quantitative description of the measured magneto-optical spectra would require one to combine the modeling of the complex, spin-orbit coupled band structure with a more detailed treatment of the strong disorder effects in (Ga,Mn)As, as previously done, e.g., in the studies of unpolarized absorption spectra [55].

ACKNOWLEDGMENTS

We thank J. Zemen and P. Motloch for providing tight-binding data for the band structure in Fig. 1 and J. Li for preliminary calculations of nondirect optical transitions in disordered crystals. Communication with R. Schäfer and V. Kamberský helped to clarify terminology. Additional measurements were performed by V. Saidl and R. Farshchi. The access to computing and storage facilities owned by parties and projects contributing to the National Grid Infrastructure MetaCentrum, provided under the program "Projects of Large Infrastructure for Research, Development, and Innovations" (LM2010005) is highly appreciated. Thanks for helpful discussions are also due to C. A. Ullrich, A. Khaetskii, A. Dirks, J. Han, I. Žutić, F. Eich, J. Wunderlich, J. Kuneš, and, very specially, to J. Mašek. Support of V.M., of the Academy of Sciences of the Czech Republic via Praemium Academiae and funding from ERC Advanced Grant No. 268066 is gratefully acknowledged. Work done at the University at Buffalo was supported by NSF-DMR1006078, by the US Department of Energy, Office of Basic Energy Sciences, Division of Materials Sciences and Engineering under Award No. DE-SC0004890 and NSF ECCS-1102092. We also acknowledge funding by FAPESP (2011/19333-4) and CNPq (246549/2012-2), MŠMT (Grant No. LM2011026), US agencies through ONR-N000141110780, NSF-DMR-1105512, Grant Agency of the Czech Republic through Grant No. P204/12/0853, and Grant Agency of Charles University in Prague through Grant No. 443011.

APPENDIX A: CLASSICAL THEORY OF MAGNETO-OPTICAL EFFECTS

Maxwell's equations allow us to show how the magneto-optical effects described in Sec. II follow from properties of the bulk magnetic material. Inspired by the argumentation of [56], we review in this appendix how MLD/MLB (or their circular counterparts), i.e., difference in imaginary/real parts of the refractive indices for two linearly (circularly) polarized modes, is calculated from bulk ac conductivity tensor of the material. The relation between these refractive indices and the particular magneto-optical effects is also explained here using simple examples and we refer the reader to Appendix C for a discussion of the more realistic relationship pertaining to our measurements.

Consider an electromagnetic wave $\vec{E}(\vec{r},t) = \vec{E}_0 e^{i(kz-\omega t)}$ propagating along $\vec{k} \parallel \hat{z}$. The nonzero ac conductivity $\sigma(\omega)$ and Maxwell equations imply that

$$\nabla(\nabla \cdot \vec{E}) - \nabla^2 \vec{E} = -\mu\sigma \dot{\vec{E}} - \mu\varepsilon \ddot{\vec{E}}, \tag{A1}$$

which yields an equation for $\vec{E}_0$ whose solutions correspond to the modes of the system. The character of these modes is determined by material parameters: permeability μ, permittivity ε, and conductivity σ tensors. The right-hand side of Eq. (A1) can be rewritten in the form $\omega^2\mu\varepsilon_{\text{eff}}\vec{E}(\vec{r},t)$ with effective permittivity written as $\varepsilon_{\text{eff}} = \varepsilon_0 + i\sigma/\omega$ where ε_0 is vacuum permittivity and σ is calculated from the response of the whole system (all electrons and crystal lattice) to perturbing electric field. When the response of only a part of the whole system is explicitly considered, as in Eq. (4), ε_0 is replaced by $\varepsilon_b\varepsilon_0$ as discussed in the text introducing that equation. We now consider two examples related to the magnetization in-plane and out-of-plane magneto-optical experiments discussed in Sec. II. The permeability μ will from now on be considered a scalar equal to the vacuum permeability and a material of cubic symmetry will be assumed whose index of refraction in the absence of magnetization equals $n_0 = \sqrt{\varepsilon_{\text{eff}}/\varepsilon_0}$.

In the first example, $\vec{M} \parallel \hat{z}$ which implies [57] an effective permittivity tensor of the form

$$\varepsilon_{\text{eff}} = \varepsilon_0 \begin{pmatrix} \varepsilon_{xx} & \varepsilon_{xy} & 0 \\ -\varepsilon_{xy} & \varepsilon_{xx} & 0 \\ 0 & 0 & \varepsilon_{zz} \end{pmatrix} \tag{A2}$$

with dimensionless components ε_{ij}. The eigenmodes obtained by solving Eq. (A1) are two circularly polarized waves with refractive indices $n_+^2 = \varepsilon_{xx} + i\varepsilon_{xy}$ and $n_-^2 = \varepsilon_{xx} - i\varepsilon_{xy}$. Consider now a slab of a magnetic material of thickness d described by ε_{eff} in Eq. (A2), assume normal incidence and, for simplicity, the absence of reflections on the sample surfaces. An incoming linearly polarized wave decomposes into two circularly polarized modes which propagate at different phase velocities. Under the additional (typically satisfied) assumption $|n_\pm - n_0| \ll n_0$, we can conclude using

$$n_+ - n_- \approx \frac{n_+^2 - n_-^2}{2n_0} = \frac{i\varepsilon_{xy}}{n_0} \tag{A3}$$

that the polarization plane of the outgoing wave will be rotated by $\theta \approx -(d\omega/c)\text{Im}\,\varepsilon_{xy}/n_0$. In the outlined geometry, the Faraday rotation is directly related to magnetic circular birefringence (MCB) while magnetic circular dichroism (MCD) will make the outgoing wave elliptically polarized ($\psi \neq 0$).

The (polar) Kerr effect is obtained by considering reflection off an interface between a semi-infinite magnetic material and vacuum. Applying the Fresnel formula for the reflection coefficient $r = (1-n)/(1+n)$ at normal incidence with $n_\pm$ defined below Eq. (A2), we obtain $r_\pm$ for the two circularly polarized modes. Polarization properties of the reflected wave can be expressed using the complex-valued ratio $r_+/r_- = ae^{i\xi}$: the originally linearly polarized wave is reflected as elliptically polarized (unless $a = 1$) with the major axis rotated by $\theta = \xi$ (see Fig. 1). In a general case, it is not possible to link MCB alone directly to the rotation and unlike with the Faraday effect, both MCB and MCD will influence θ because the relation between r and n is nonlinear. An illustrative example of this is given in Appendix C.

In the second example $\vec{M} \parallel \hat{x}$, which implies the same form of ε_{eff} as in Eq. (A2) up to a permutation of indices. Solving Eq. (A1) for $\vec{E}_0$ gives

$$\begin{pmatrix} E_x^0 \\ E_y^0 \\ E_z^0 \end{pmatrix} \propto \begin{pmatrix} 1 \\ 0 \\ 0 \end{pmatrix} \text{ and } \begin{pmatrix} 0 \\ 1 \\ \varepsilon_{yz}/\varepsilon_{zz} \end{pmatrix} \tag{A4}$$

with refractive indices $n_\parallel^2 = \varepsilon_{xx}$ and $n_\perp^2 = \varepsilon_{zz}[1 + (\varepsilon_{yz}/\varepsilon_{zz})^2]$. Voigt rotation [after transmission through a slab of the magnetic material as sketched in Fig. 2(b)] is related to

$$n_\parallel - n_\perp \approx \frac{1}{2} n_0 \left(\varepsilon_{xx} - \varepsilon_{zz} - \frac{\varepsilon_{yz}^2}{\varepsilon_{zz}} \right) \tag{A5}$$

in analogy to Eq. (A3). The ellipsometric parameters for the Voigt effect in reflection are evaluated as follows. First the dimensionless parameter is calculated:

$$\chi = \frac{r(n_\parallel) - r(n_\perp)}{r(n_\parallel) + r(n_\perp)}. \tag{A6}$$

Then the rotation and ellipticity angles are

$$\theta = \frac{1}{2} \text{atan} \left(\frac{2\text{Re}\ \chi}{1 - |\chi|^2} \right) \quad \psi = \frac{1}{2} \text{asin} \left(\frac{2\text{Im}\ \chi}{1 + |\chi|^2} \right). \tag{A7}$$

Assuming $\beta = \pi/4$ and $b = r_\parallel / r_\perp$ real for simplicity, we get

$$\tan\theta = \frac{1-b}{1+b} \approx \frac{n_0}{2(n_0^2 - 1)} \left(\varepsilon_{xx} - \varepsilon_{zz} - \frac{\varepsilon_{yz}^2}{\varepsilon_{zz}} \right). \tag{A8}$$

For other mutual positions of $\vec{M}$ and polarization plane, θ will follow the $\sin 2\beta$ dependence as mentioned in Sec. II. In particular, when incident beam polarization is parallel or perpendicular to $\vec{M}$, light in the magnetic material travels simply as the first or second mode in (A4) and the polarization remains unchanged.

With these two examples at hand, we can make several observations. Recall that we have always considered the normal incidence here. The in-plane magnetization leads to magneto-optical effects even in magnetization, $\theta(\vec{M}) = \theta(-\vec{M})$, as stated in Sec. II. In Eq. (A5), $\varepsilon_{xx} - \varepsilon_{zz}$ is even in $\vec{M}$ owing to the Onsager relations, and ε_{yz}^2 is even because $\varepsilon_{yz}(\vec{M})$ is odd [58]. Next, we can see that a nonzero difference between $n_\parallel$ and $n_\perp$ in nondissipative systems ($\text{Im}\ n_\parallel = \text{Im}\ n_\perp = 0$), a circumstance that could be called "pure MLB," causes rotation in the Voigt effect in reflection. However, as soon as $n_\parallel$ and $n_\perp$ are complex, both MLB and MLD will influence θ because of the nonlinear dependence of r on n. We again refer to the illustrative example given in Appendix C. A similar statement holds about ellipticity of the Voigt effect in reflection. Some confusion can arise because of different terminology used in the literature: Reference [1] relates MLB to the real part of refractive indices while [4] relates to the real part of the reflection coefficients. We find the former terminology more appropriate because it is generic for both reflection and transmission coefficients. Independent of the terminology, it is safe to state that different complex refractive indices $n_\parallel$ and $n_\perp$ cause $\theta \neq 0$, $\psi \neq 0$ in both transmission and reflection experiments. Nonzero $n_\parallel - n_\perp$ arises due to a difference in diagonal components of ε_{eff} or nonzero ε_{yz}, as seen in Eq. (A5). Since $\varepsilon_{yz}^2/\varepsilon_{zz}$ is in our case negligible [59], one can conclude that the Voigt effect in reflection or in transmission is (via MLB and MLD) primarily driven by the difference of diagonal components of $\sigma(\omega)$ corresponding to directions parallel and perpendicular to $\vec{M}$, i.e., by the ac anisotropic magnetoresistance.

We conclude this appendix by explaining the relationship between terminology used in this paper (components of the effective permittivity tensor ε_{eff}) and the notation of "quadratic magneto-optic tensor components" [60,61] used elsewhere [62–64]. The basic conceptual difference between the two approaches is whether $\vec{M}$ is kept fixed and different polarizations of light are considered (the former approach) or vice versa (the latter approach). An advantage of the latter approach is its aptitude to describe the ac analogy of crystalline anisotropic magnetoresistance components [65] which we completely ignore in this paper, motivated by their smallness in the dc limit [10]. We expand the effective permittivity tensor into a Taylor series in powers of the magnetization Cartesian components M_k:

$$\varepsilon_{ij} = \varepsilon_{ij}^{(0)} + K_{ijk} M_k + G_{ijkl} M_k M_l + \cdots, \tag{A9}$$

where $\varepsilon_{ij}^{(0)}$ is the part independent on magnetization, K_{ijk} and G_{ijkl} are rank 3 and 4 tensors, and the last two are sometimes also called linear and quadratic magneto-optical tensors. They represent the parts of the permittivity tensor which are linear and quadratic in magnetization, respectively.

The form of K_{ijk} and G_{ijkl} depends on the symmetry of the crystal [61] as well as on the orientation of principal crystal axis with respect to the xyz axis in which the permittivity tensor is expressed [64]. In the case of cubic crystals with point symmetry (crystal classes $23 = T$, $m3 = T_h$, $432 = O$, $\bar{4}3m = T_d$, and $m3m = O_h$), where $\langle 100 \rangle$, $\langle 010 \rangle$, and $\langle 001 \rangle$ are parallel with x, y, and z axis, respectively, the following three statements hold. The nonmagnetic part of the permittivity tensor is constant, $\varepsilon_{ij}^{(0)} = \delta_{ij} \varepsilon^{(0)}$, where δ_{ij} is the Kronecker δ. The third-rank tensor $K_{ijk} = \gamma_{ijk} K$ where γ_{ijk} is Levi-Civita symbol. The rank-4 tensor G_{ijkl} can be written in matrix form as [61]

$$\begin{pmatrix} \varepsilon_{xx}^{(2)} \\ \varepsilon_{yy}^{(2)} \\ \varepsilon_{zz}^{(2)} \\ \varepsilon_{yz}^{(2)} \\ \varepsilon_{zx}^{(2)} \\ \varepsilon_{xy}^{(2)} \end{pmatrix} = \begin{pmatrix} G_{11} & G_{12} & G_{12} & 0 & 0 & 0 \\ G_{12} & G_{11} & G_{12} & 0 & 0 & 0 \\ G_{12} & G_{12} & G_{11} & 0 & 0 & 0 \\ 0 & 0 & 0 & 2G_{44} & 0 & 0 \\ 0 & 0 & 0 & 0 & 2G_{44} & 0 \\ 0 & 0 & 0 & 0 & 0 & 2G_{44} \end{pmatrix} \times \begin{pmatrix} M_x^2 \\ M_y^2 \\ M_z^2 \\ M_y M_z \\ M_z M_x \\ M_x M_y \end{pmatrix}, \tag{A10}$$

where $\varepsilon_{ij}^{(2)} = G_{ijkl} M_k M_l$. In the case of an isotropic material, the number of free parameters is further reduced because $2G_{44} = G_{11} - G_{12}$.

In our analysis in Sec. IV, magnetization was always oriented along the x axis and combining Eqs. (A10) and (A9), we arrive at

$$\varepsilon = \begin{pmatrix} \varepsilon^{(0)} + G_{11}M_x^2 & 0 & 0 \\ 0 & \varepsilon^{(0)} + G_{12}M_x^2 & KM_x \\ 0 & -KM_x & \varepsilon^{(0)} + G_{12}M_x^2 \end{pmatrix}. \tag{A11}$$

Repeating the analysis leading to Eq. (A5), we now find $n_\parallel - n_\perp = (G_{11} - G_{12} - K^2/\varepsilon^{(0)})M_x^2$.

APPENDIX B: MICROSCOPIC MODEL

This appendix contains detailed information about the model of (Ga,Mn)As electronic structure embodied in Eq. (3), its parameters, and the Kubo formula used to calculate conductivity tensor components entering Eq. (B4).

Individual samples are primarily characterized by the Mn doping x (fraction of Ga atoms substituted by Mn) and total hole density p. The former is taken as $x = N_{\mathrm{Mn}}a_l^3/4$ where $a_l = 0.565\,325$ nm is the GaAs lattice constant and N_{Mn} is the density of Mn atoms. Since Mn substituting for a Ga atom is a single acceptor, it follows $p = N_{\mathrm{Mn}}$ and $|\vec{M}| = 5\mu_B N_{\mathrm{Mn}}$ in the ideal case [for the moment, we neglect magnetic moment of the holes, included in Eq. (B1) below]. However, compensating impurities (e.g., As antisites or Mn atoms in interstitial position) will reduce both p and magnetization $|\vec{M}|$. These two quantities therefore have to be determined independently by measurement as is done in Fig. 10 and Table I of the Supplemental Information in [16]. For our paper, the nominal doping x_{nom} serves only as a convenient "label" of the samples summarized in Table I. We take p directly from [16] and using the values of M_{sat} from the same source, we calculate the effective doping

$$x = \frac{M_{\mathrm{sat}}a_l^3}{8(S_{\mathrm{Mn}} + S_{\mathrm{carr}})\mu_B}, \tag{B1}$$

which is also given in Table I. The Mn magnetic moment $S_{\mathrm{Mn}} = 5/2$ dominates M_{sat}, carriers contribute by a smaller part, and we take $S_{\mathrm{carr}} = -0.25$ because the (incompletely polarized [66]) hole spins are oriented antiparallel to those of the Mn. Using this x, we calculate $M = |\vec{M}|$ in Eq. (3) as $8xS_{\mathrm{Mn}}\mu_B/a_l^3$. Note that Eq. (B1) basically expresses the notion that in annealed metallic samples there are approximately 4.5 Bohr magnetons per manganese atom [67]. We also note that the hole concentration $4x/a_l^3$ corresponding to Eq. (B1) is sometimes lower than the one determined from the Hall measurements (see Table I). This bears witness to the inaccuracies of the experimental methods used to determine the material parameters as already explained in the Supplemental Information of [16].

Our $\hat{H}_{\mathrm{KL}}$ in Eq. (3) is the eight-band Kohn-Luttinger Hamiltonian identical to the corresponding block in Eq. (2) of [68]. We use GaAs Luttinger parameters $\gamma_{1/2/3} = 6.98/2.06/2.93$ together with $\Delta_{SO} = 341$ meV, $E_g = 1.519$ eV, $E_P = 2m_0P^2/\hbar^2 = 24.8$ eV, $m_c^* = 0.067m_0$ where m_0 is the electron vacuum mass. The middle two terms in Eq. (3) describe the ferromagnetic splitting in our model. When $\vec{M}||\hat{x}$, as we always assume in our calculations, they combine into an 8×8 matrix $h\hat{m}$ where

$$\hat{m} = \begin{pmatrix} 0 & 0 & \frac{\sqrt{3}}{2} & 0 & \frac{\sqrt{3}}{\sqrt{2}} & 0 & 0 & 0 \\ 0 & 0 & 1 & \frac{\sqrt{3}}{2} & \frac{-1}{\sqrt{2}} & 0 & 0 & 0 \\ \frac{\sqrt{3}}{2} & -1 & 0 & 0 & 0 & \frac{-1}{\sqrt{2}} & 0 & 0 \\ 0 & \frac{\sqrt{3}}{2} & 0 & 0 & 0 & -\frac{\sqrt{3}}{\sqrt{2}} & 0 & 0 \\ \frac{\sqrt{3}}{\sqrt{2}} & \frac{1}{\sqrt{2}} & 0 & 0 & 0 & \frac{1}{2} & 0 & 0 \\ 0 & 0 & \frac{1}{\sqrt{2}} & \frac{\sqrt{3}}{\sqrt{2}} & -\frac{1}{2} & 0 & 0 & 0 \\ 0 & 0 & 0 & 0 & 0 & 0 & 0 & \eta \\ 0 & 0 & 0 & 0 & 0 & 0 & \eta & 0 \end{pmatrix} \tag{B2}$$

with $\eta = J_{sd}/J_{pd}$ and the prefactor $h = J_{pd}M/\mu_B$. The kinetic-exchange couplings are $J_{pd} = 55$ meV nm^3 and $J_{sd} = -9.2$ meV nm^3. By diagonalizing $\hat{H}$ of Eq. (3) in each $\vec{k}$ point of a suitably chosen mesh around the Γ point of the Brillouin zone, we obtain band dispersions $E_{a\vec{k}}$ and corresponding spinors $|a,\vec{k}\rangle$.

We now describe the many-body corrections $\hat{V}_{xc}$ in Eq. (3). Since the exchange energy per particle of free spin-polarized electrons,

$$E_x/N = -\frac{e^2}{4\pi\epsilon}\frac{3k_F}{4\pi}, \tag{B3}$$

is of the order of 100 meV at carrier densities of the order of 10^{21} cm^{-3}, such corrections are relevant in the analysis of the α-peak position (keep in mind that the discrepancy between experimental and theoretical peak positions in Fig. 6 are of this order of magnitude).

The difficulty in evaluating the exchange-correlation effects for the holes is in the presence of a strong spin-orbit coupling. One possible approximative scheme is discussed in [69]. To assess the qualitative effect of exchange energy on trends in the rotation spectra of the Voigt effect in reflection, we use the following scheme. We first disregard the correlation effects which are small compared to exchange in Eq. (B3). For given x and p, we first determine the band occupations by holes p_i ($\Sigma_i p_i = p$, $i = 1,\ldots,6$) as given by Eq. (3) with $V_{xc} = 0$. For most of the considered dopings, only the LH ($i = 3,4$) and HH bands ($i = 5,6$) are occupied by holes. We next recalculate the corresponding densities p_i into Fermi wave vectors assuming isotropic dispersion and shift the bands by $-E_x/N$ as given by Eq. (B3). Since $-E_x/N$ is different for different bands, this procedure not only renormalizes the Fermi level but also slightly changes p_i and therefore we iterate the procedure until we converge to a consistent set of p_i and exchange shifts. Note that we neglected in this procedure the exchange between bands $i \neq j$. To justify this approximation, at least in part, we checked the spin polarizations of individual bands. For example, $x = 3\%$, $p = 0.6 \times 10^{21}$ cm^{-3} leads to $p_{3,4,5,6}/p = 0.02,0.04,0.33,0.61$ and integral spin polarizations $2\langle s\rangle_{3,4,5,6} = 0.58,-0.14,0.57,-0.91$. The majority HHs are thus prevalent and nearly completely polarized, hence their exchange interaction with holes in other bands will be small and our estimate using Eq. (B3) with $k_F^3 = 6\pi^2 p_6$ should be a good approximation. On the other hand, the exchange shifts for LH bands may contain sizable corrections due to the neglected interband exchange and the values 52, 62, 126, and 154 meV thus serve only as a rough guide to assess many-body

effects on the magneto-optical spectra. These values are similar to the band-gap renormalization [70] used previously [6]. A commonly considered correction to Eq. (B3) capturing part of the correlation effects is logarithmic and weakly dependent on p in our range of parameters. Appealing to the second term in Eq. (36) of [69] and the procedure described therein, we include it into our model through a small constant shift of 6.5 meV (1.5 meV) for HH (LH) bands towards the conduction bands. To summarize many-body corrections included in Eq. (3), $\hat{V}_{xc}$ can be understood as a single-particle operator that commutes with $\hat{H}$ and shifts the selected bands as just described to account for exchange and partly also correlations. This approximative treatment enhances the ferromagnetic splitting between minority and majority hole bands and also adds an additional offset between the HH and LH bands.

The charge density of the delocalized holes is not constant as in the jellium model and this causes an additional band-gap renormalization that can be described by the real part of self-energy due to hole-acceptor scattering [70]. We estimate it by Eq. (5) of this reference with $g = 1$ (full spin polarization of the holes) and HH effective mass of half the free electron mass as an additional shift of the valence bands towards the conduction bands added to $\hat{V}_{xc}$. Positions of the peak α redshift by an additional [16] ∼300 meV which still leaves the calculated positions of peak α in Fig. 6 several hundreds of meV above the experimental data.

These three ingredients can be used to calculate the conductivity tensor components

$$\sigma_{jl}(\omega) = \sigma_{jl}^{\text{intra}} + \sigma_{jl}^{\text{inter}} \tag{B4}$$

whose intraband part is taken to be $\propto\delta_{jl}$,

$$\sigma_{jj}^{\text{intra}} = \sum_n \frac{\sigma_0^{j,n}(1 + i\hbar\omega/\Gamma)}{1 + (\hbar\omega/\Gamma)^2}. \tag{B5}$$

It contains only the diagonal matrix elements of the velocity operator $\hat{v}_j$ ($j = x,y,z$ denotes its Cartesian component) appearing in the dc Drude conductivity $\sigma_0^{j,n}$ along a given direction in the nth band. Relaxation times [71] corresponding to $\Gamma = 100$ meV are assumed to be n and $\vec{k}$ independent. Off-diagonal components $\sigma_{ij}^{\text{intra}}$ are not calculated, since they contribute only little to the Voigt effect in reflection [59]. Due to the combined effect of the ferromagnetic splitting (keep in mind that $\vec{M}||\hat{x}$) and spin-orbit interaction, there is a small difference between $\sigma_0^{x,n}$ and $\sigma_0^{z,n}$. Additionaly, Eq. (B5) does not take into account anisotropy induced by external magnetic field which is used in experiments to control $\vec{M}$. Both effects lead to a small anisotropy in $\sigma_{ii}^{\text{intra}}$ which we estimated to have only negligible effect on the resulting spectra of $\theta(\omega)$ and $\psi(\omega)$.

Off-diagonal matrix elements $v_j^{ab\vec{k}\vec{k}'} = \langle a,\vec{k}|\hat{v}_j|b,\vec{k}'\rangle$ enter through the interband part of Eq. (B4) for which we use

$$\sigma_{jl}^{\text{inter}} = -\frac{i\hbar e^2}{V}\sum_{\vec{k},\vec{k}',a,b}[f(E_{a\vec{k}}) - f(E_{b\vec{k}})] \times \frac{v_j^{ab\vec{k}\vec{k}'}v_l^{ba\vec{k}'\vec{k}}}{(E_{a\vec{k}} - E_{b\vec{k}'} + i\Gamma)(E_{a\vec{k}} - E_{b\vec{k}'} - \hbar\omega + i\Gamma)}, \tag{B6}$$

where $f(E)$ is the Fermi-Dirac distribution function that contains the Fermi level E_f determined from the total hole concentration p and V is the system volume. The conservation of $\vec{k}$ vector in optical transitions, $v_j^{ab\vec{k}\vec{k}'}, v_l^{ba\vec{k}'\vec{k}} \propto \delta_{\vec{k}\vec{k}'}$, is a property of perfect crystals. Derivation of Eq. (B6) follows [73] and the Appendix of [74] and details pertaining both to Eqs. (B6) and (B5) can be found in [48].

APPENDIX C: FROM CONDUCTIVITY TO THE VOIGT EFFECT IN REFLECTION

Typical $\sigma_\parallel \equiv \sigma_{xx}$, $\sigma_\perp \equiv \sigma_{yy}$ as of Eq. (B4) are shown in Figs. 7(a) and 7(b) (real and imaginary parts). The angle θ (and similarly ψ) is according to Eq. (A8) related to their difference $\sigma_\parallel - \sigma_\perp$ and we therefore also plot this quantity. Some spectral features of Fig. 5(a) can be seen in Fig. 7(c) (Re $\sigma_\parallel - \sigma_\perp$) and Fig. 7(d) (Im $\sigma_\parallel - \sigma_\perp$) but their relationship is not straightforward.

Once the optical conductivities $\sigma_\parallel(\omega)$ and $\sigma_\perp(\omega)$ are known, effective permittivity and refractive indices can be calculated using Eq. (4),

$$\begin{aligned} n_\parallel^2 &= \mu\varepsilon_{\text{eff}}^\parallel = \mu\left(\varepsilon_b + \frac{i\sigma_{||}}{\omega}\right), \\ n_\perp^2 &\approx \mu\varepsilon_{\text{eff}}^\perp = \mu\left(\varepsilon_b + \frac{i\sigma_\perp}{\omega}\right), \end{aligned} \tag{C1}$$

where μ is the relative permeability which we take $\mu = 1$. The $\varepsilon_{yz}^2/\varepsilon_{zz}$ term contributing to $n_\perp$ according to Eq. (A5) can be neglected [59]: diagonal components of permittivity are dominated by the background ε_b and this large value causes σ_{yz}/σ_b^2 (with $\sigma_b = 1500\ (\Omega\,\text{cm})^{-1}$ appropriate for $\varepsilon_b \approx 10.9$) to be small compared to $\sigma_\parallel - \sigma_\perp$ as shown in the lower panels of Fig. 7. Since both real and imaginary parts of $n_\parallel$ and $n_\perp$ differ, meaning that both (magnetic linear) birefringence and dichroism are present in our system, let us consider an illustrative example of how MLD and MLB individually

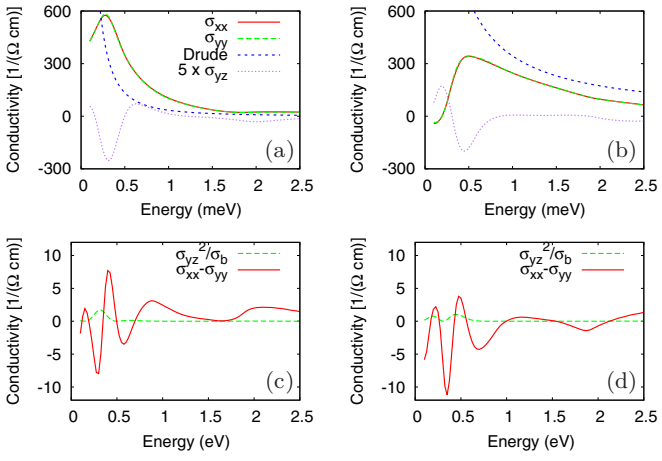

FIG. 7. (Color online) Conductivities σ_{xx}, $\sigma_{yy} = \sigma_{zz}$, and σ_{yz} (magnetization along $\hat{x}$) corresponding to $p = 10^{21}$ cm^{-3} and $x = 5\%$. (a) Real and (b) imaginary part of the interband conductivities according to Eq. (B6); intraband (Drude) part is also shown. Note that the off-diagonal conductivity is magnified by a factor of 5. (c),(d) Real/imaginary part of the difference between diagonal components. The relatively small (Re $\sigma_{yz})^2/\sigma_b$ and (Im $\sigma_{yz})^2/\sigma_b$ with $\sigma_b = 1500\ (\Omega\,\text{cm})^{-1}$ are also shown in panels (c) and (d).

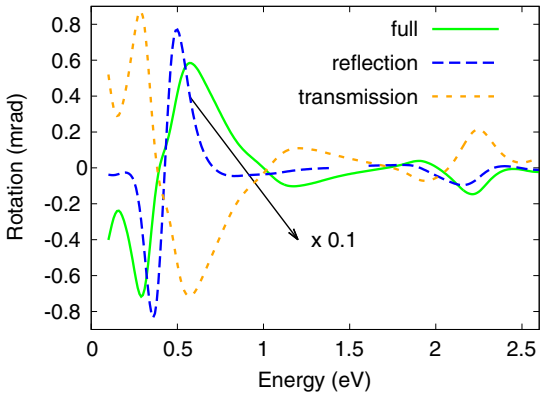

FIG. 8. (Color online) Rotation for a sample with $p = 0.4 \times 10^{21}$ cm^{-3}, $x = 5\%$, and $d = 20$ nm in three situations: transmission (i.e., Voigt effect), reflection from a thick layer ($d \to \infty$) and geometry of our measurements (labeled "full"). Note that the dashed curve is downscaled by a factor of 10 in the range $\hbar\omega < 1.5$ eV.

influence the resultant θ. Assume that $\varepsilon_{xx} = 11.60 + 0.70i$ and $\varepsilon_{zz} = 11.61 + 0.71i$; this is inspired by values in Fig. 7 and it would correspond to $\sigma \approx 100\ (\Omega\,\mathrm{cm})^{-1}$ at $\hbar\omega = 1$ eV and $|\sigma_{xx} - \sigma_{zz}|$ of the order of 1 $(\Omega\,\mathrm{cm})^{-1}$. The rotation $\theta \approx \mathrm{Re}\,\chi$, as given by Eq. (A7), will be 0.151 mrad if reflection on an infinitely thick (Ga,Mn)As layer is considered. Now consider the pure MLD situation: $\varepsilon_{xx} = 11.60 + 0.70i$ and $\varepsilon_{zz} = 11.60 + 0.71i$ would give $\theta = 0.009$ mrad. On the other hand, $\varepsilon_{xx} = 11.60 + 0.70i$ and $\varepsilon_{zz} = 11.61 + 0.70i$ (pure MLB) results in $\theta = 0.142$ mrad. It is clear that both MLD and MLB can significantly contribute to the spectra of rotation of the Voigt effect in reflection.

Taking into account the effect of the substrate as in Fig. 3 and Eq. (5) of [5], (Ga,Mn)As refractive index n leads to the reflection coefficient

$$r(n) = \frac{(n_s - 1)\cos(kd) - i(n - n_s/n)\sin(kd)}{(n_s + 1)\cos(kd) - i(n + n_s/n)\sin(kd)}. \qquad \text{(C2)}$$

Using Eqs. (C1) and (C2) we get $r(n_\parallel)$ and $r(n_\perp)$ that can be inserted into Eq. (A6) and we finally obtain the rotation and ellipticity θ, ψ. Multiple reflections in a (Ga,Mn)As layer are taken into account in Eq. (C2); the complex $k = n\omega/c$, the layer has a finite thickness d, and it is sandwiched between vacuum and GaAs substrate with refractive indices 1 and $n_s = \sqrt{\varepsilon_b + i\sigma_{\mathrm{GaAs}}/\omega\varepsilon_0}$, respectively. As was explained below Eq. (4), we use ω-dependent ε_b which, together with intrinsic GaAs ac conductivity $\sigma_{\mathrm{GaAs}}(\omega)$ calculated from Eq. (B6), reproduces the experimentally known refractive index of GaAs. This seemingly over-cautious method of determining n_s is important for maintaining the consistency of our optical model in Eq. (C2). It guarantees that in the $x \to 0$, $p \to 0$ limit applied to our (Ga,Mn)As layer, reflection from the layer/substrate interface will be zero.

Indeed, multilayer optical properties significantly influence the final form of the spectra (experimentally, thickness dependence of θ at $\hbar\omega = 1.58$ eV was studied by Al-Qadi *et al.* in [75]). Figure 8 shows that differences between the transmission and reflection Voigt effect experiments could be significant, yet the spectral features (and their position in particular) remain to some extent unaffected. For example, peak α is somewhat suppressed in pure reflection (dashed curve in Fig. 8) that would correspond to an experiment with a thick layer ($d \to \infty$). Features β, γ in the subgap energy range would, however, be order of magnitude larger in pure reflection. A hypothetical experiment measuring transmission (including multireflections) through a thin ($d = 20$ nm) layer would give the Voigt effect as shown by the dotted curve where, roughly speaking, the spectrum only changes the overall sign. Multiple reflections between the substrate-sample and air-sample interfaces substantially modify the spectra although their effect may even be somewhat exaggerated in our model. Based on an estimate $\mathrm{Re}\,\sigma_{xx} = \mathrm{Im}\,\sigma_{xx} = 200\ (\Omega\,\mathrm{cm})^{-1}$ at $\hbar\omega = 1$ eV (compare Fig. 7), we obtain index of refraction $n \approx 1.2$ and therefore a large reflection coefficient at the substrate/sample interface. With absorption coefficients $\alpha(\omega) \sim 10\,000$ cm^{-1}, i.e., $\alpha d \approx 0.01 \ll 1$, the wave will be (in our model) able to travel many times through the sample. Experimental comparison of the effect in samples with different thicknesses however suggests that both αd is larger and the sample/substrate contrast is lower (n/n_s closer to 1).

[1] J. Ferre and G. A. Gehring, Rep. Prog. Phys. **47**, 513 (1984).
[2] T. Jungwirth, J. Sinova, J. Mašek, J. Kučera, and A. H. MacDonald, Rev. Mod. Phys. **78**, 809 (2006).
[3] K. S. Burch, J. Stephens, R. K. Kawakami, D. D. Awschalom, and D. N. Basov, Phys. Rev. B **70**, 205208 (2004).
[4] A. V. Kimel, G. V. Astakhov, A. Kirilyuk, G. M. Schott, G. Karczewski, W. Ossau, G. Schmidt, L. W. Molenkamp, and T. Rasing, Phys. Rev. Lett. **94**, 227203 (2005).
[5] M.-H. Kim, G. Acbas, M.-H. Yang, I. Ohkubo, H. Christen, D. Mandrus, M. A. Scarpulla, O. D. Dubon, Z. Schlesinger, P. Khalifah *et al.*, Phys. Rev. B **75**, 214416 (2007).
[6] G. Acbas, M.-H. Kim, M. Cukr, V. Novák, M. A. Scarpulla, O. D. Dubon, T. Jungwirth, J. Sinova, and J. Cerne, Phys. Rev. Lett. **103**, 137201 (2009).
[7] N. Nagaosa, J. Sinova, S. Onoda, A. H. MacDonald, and N. P. Ong, Rev. Mod. Phys. **82**, 1539 (2010).
[8] R. Schäfer and A. Hubert, Phys. Status Solidi A **118**, 271 (1990).
[9] S. Kokado, M. Tsunoda, K. Harigaya, and A. Sakuma, J. Phys. Soc. Jpn. **81**, 024705 (2012).
[10] A. W. Rushforth, K. Výborný, C. S. King, K. W. Edmonds, R. P. Campion, C. T. Foxon, J. Wunderlich, A. C. Irvine, P. Vašek, V. Novák *et al.*, Phys. Rev. Lett. **99**, 147207 (2007).
[11] A. Kirilyuk, A. V. Kimel, and T. Rasing, Rev. Mod. Phys. **82**, 2731 (2010).
[12] A. V. Kimel, A. Kirilyuk, A. Tsvetkov, R. V. Pisarev, and T. Rasing, Nature (London) **429**, 850 (2004).
[13] P. Wadley, Nat. Commun. **4**, 2322 (2013).
[14] H.-C. Mertins, P. M. Oppeneer, J. Kuneš, A. Gaupp, D. Abramsohn, and F. Schäfers, Phys. Rev. Lett. **87**, 047401 (2001).
[15] K. Ando, T. Hayashi, M. Tanaka, and A. Twardowski, J. Appl. Phys. **83**, 6548 (1998).

[16] T. Jungwirth, P. Horodyská, N. Tesařová, P. Němec, J. Šubrt, P. Malý, P. Kužel, C. Kadlec, J. Mašek, I. Němec *et al.*, Phys. Rev. Lett. **105**, 227201 (2010).

[17] G. P. Moore, J. Ferre, A. Mougin, M. Moreno, and L. Daweritz, J. Appl. Phys. **94**, 4530 (2003).

[18] N. Tesařová, J. Šubrt, P. Malý, P. Němec, C. T. Ellis, A. Mukherjee, and J. Cerne, Rev. Sci. Instrum. **83**, 123108 (2012).

[19] M. Abolfath, T. Jungwirth, J. Brum, and A. H. MacDonald, Phys. Rev. B **63**, 054418 (2001).

[20] H. Ebert, Rep. Prog. Phys. **59**, 1665 (1996).

[21] Cyclotron resonance (in nonmagnetic materials) gives rise to a peak in absorption which shifts with increasing magnetic field [22]. The term "magnetooptics" also commonly embraces this effect.

[22] M. Orlita, W. Escoffier, P. Plochocka, B. Raquet, and U. Zeitler, C. R. Phys. **14**, 78 (2013).

[23] M. Buchmeier, R. Schreiber, D. E. Bürgler, and C. M. Schneider, Phys. Rev. B **79**, 064402 (2009).

[24] Hubert and Schäfer [8] (HS) observed an effect related to magnetization gradient while studying in-plane magnetized domains of magnetic thin films. It was later named the HS effect [25] but since the original reference [8] also reports on the observation of the Voigt effect in reflection, terminology became somewhat confused. Boundary effects in systems with magnetic domains (and nonzero magnetic gradients) naturally receive the name HS effect [26] but the x-ray Voigt effect in reflection off thin iron layers with homogeneous magnetization has also been called the HS effect [27]. In the present paper, we adhere to the original convention [8] and use the term "Voigt effect in reflection."

[25] V. Kamberský, J. Magn. Magn. Mater. **104–107**, 311 (1992).

[26] I. Banno, Phys. Rev. A **77**, 033818 (2008).

[27] S. Valencia, A. Kleibert, A. Gaupp, J. Rusz, D. Legut, J. Bansmann, W. Gudat, and P. M. Oppeneer, Phys. Rev. Lett. **104**, 187401 (2010).

[28] E. A. Gan'shina, A. V. Zenkov, G. S. Krinchik, A. S. Moskvin, and A.Yu. Trifonov, Sov. Phys. JETP **72**, 154 (1991).

[29] V. I. Belotelov *et al.*, Opt. Lett. **34**, 398 (2009).

[30] K. Postava, H. Jaffres, A. Schuhl, F. N. V. Dau, M. Goiran, and A. Fert, J. Magn. Magn. Mater. **172**, 199 (1997).

[31] P. Němec, V. Novák, N. Tesařová, E. Rozkotová, H. Reichlová, D. Butkovičová, F. Trojánek, K. Olejník, P. Malý, R. P. Campion *et al.*, Nat. Commun. **4**, 1422 (2013).

[32] J. Zemen, J. Kucera, K. Olejnik, and T. Jungwirth, Phys. Rev. B **80**, 155203 (2009).

[33] M.-H. Kim, V. Kurz, G. Acbas, C. T. Ellis, and J. Cerne, J. Opt. Soc. Am. B **28**, 199 (2011).

[34] The longitudinal Kerr effect depends in a complicated manner on the angle of incidence ϕ. For small ϕ, it vanishes as [35] $\sin\phi \propto \phi$. Based on previous measurements of the magnetic circular dichroism [16,36] (polar Kerr effect), we find that the contribution of the longitudinal Kerr effect to the polarization plane rotation is small in our measurements.

[35] C.-Y. You and S.-C. Shin, Appl. Phys. Lett. **69**, 1315 (1996).

[36] P. Němec *et al.*, Nat. Phys. **8**, 411 (2012).

[37] K. Sato, Jpn. J. Appl. Phys. **20**, 2403 (1981).

[38] N. Tesařová, P. Němec, E. Rozkotová, J. Šubrt, H. Reichlová, D. Butkovičová, F. Trojánek, P. Malý, V. Novák, and T. Jungwirth, Appl. Phys. Lett. **100**, 102403 (2012).

[39] J. Hamrle, S. Blomeier, O. Gaier, B. Hillebrands, H. Schneider, G. Jakob, K. Postava, and C. Felser, J. Phys. D: Appl. Phys. **40**, 1563 (2007).

[40] E. Oh, D. U. Bartholomew, A. K. Ramdas, J. K. Furdyna, and U. Debska, Phys. Rev. B **44**, 10551 (1991).

[41] J.-M. Jancu, R. Scholz, F. Beltram, and F. Bassani, Phys. Rev. B **57**, 6493 (1998).

[42] H. B. Bebb, Phys. Rev. **185**, 1116 (1969).

[43] B. C. Chapler, S. Mack, R. C. Myers, A. Frenzel, B. C. Pursley, K. S. Burch, A. M. Dattelbaum, N. Samarth, D. D. Awschalom, and D. N. Basov, Phys. Rev. B **87**, 205314 (2013).

[44] T. Dietl, H. Ohno, F. Matsukura, J. Cibert, and D. Ferrand, Science **287**, 1019 (2000).

[45] T. Jungwirth, J. Sinova, A. H. MacDonald, B. L. Gallagher, V. Novák, K. W. Edmonds, A. W. Rushforth, R. P. Campion, C. T. Foxon, L. Eaves *et al.*, Phys. Rev. B **76**, 125206 (2007).

[46] P. Lautenschlager, M. Garriga, S. Logothetidis, and M. Cardona, Phys. Rev. B **35**, 9174 (1987).

[47] Experimentally, the permittivity of intrinsic GaAs approaches $\varepsilon_\infty = 10.9$ above the optical phonon resonance ($\hbar\omega \approx 30$ meV); see for instance C. J. Johnson, G. H. Sherman, and R. Weil, Appl. Opt. **8**, 1667 (1969). This energy is well below the lowest energies studied in our experiments.

[48] N. Tesarova, T. Ostatnicky, V. Novak, K. Olejnik, J. Subrt, C. T. Ellis, A. Mukherjee, J. Lee, G. M. Sipahi, J. Sinova, J. Hamrle, T. Jungwirth, P. Nemec, J. Cerne, and K. Vyborny, arXiv:1308.5907.

[49] T. Jungwirth, M. Abolfath, J. Sinova, J. Kučera, and A. H. MacDonald, Appl. Phys. Lett. **81**, 4029 (2002); T. Jungwirth, J. Sinova, K. Y. Wang, K. W. Edmonds, R. P. Campion, B. L. Gallagher, C. T. Foxon, Q. Niu, and A. H. MacDonald, *ibid.* **83**, 320 (2003); K. Výborný, J. Kučera, J. Sinova, A. W. Rushforth, B. L. Gallagher, and T. Jungwirth, Phys. Rev. B **80**, 165204 (2009).

[50] R. Zallen, *The Physics of Amorphous Solids* (Wiley, New York, 1983).

[51] Comparing (Ga,Mn)As to amorphous GaAs, it should be mentioned that chemical rather than structural disorder has also other ramifications than the inapplicability of Bloch theorem. The hybridization between p-like orbitals of GaAs with d-like Mn orbitals of course does change the orbital character of the valence band to some extent, so that the matrix elements in Eq. (B6) will be modified. In particular, the parameter $E_P = 2m_0P^2/\hbar^2$ mentioned above Eq. (B2) will bear witness to the modified orbitals through $P = \hbar/m_0\langle S|\hat{p}_z|X\rangle$ and optical transition probabilities will naturally also be modified. This effect is "hidden" behind the Schrieffer-Wolff transformation included in the model of [19]. Consequently, heights of the peaks in $\theta(\omega)$ will change.

[52] J. H. D. da Silva, R. R. Campomanes, D. M. G. Leite, F. Orapunt, and S. K. O'Leary, J. Appl. Phys. **96**, 7052 (2004).

[53] T. S. Moss, Proc. Phys. Soc. Sect. B **67**, 775 (1954).

[54] E. Burstein, Phys. Rev. **93**, 632 (1954).

[55] S.-R. Eric Yang, J. Sinova, T. Jungwirth, Y. P. Shim, and A. H. MacDonald, Phys. Rev. B **67**, 045205 (2003).

[56] R. Osgood III, S. Bader, B. Clemens, R. White, and H. Matsuyama, J. Magn. Magn. Mater. **182**, 297 (1998).

[57] A derivation based on the analogy between $\vec{M}$ and $\vec{B}$ is given in [56].

[58] Onsager relations imply $\varepsilon_{ij}(\vec{M}) = \varepsilon_{ji}(-\vec{M})$. For $\vec{M}||\hat{x}$, $\varepsilon_{yz}(\vec{M}) = -\varepsilon_{yz}(-\vec{M})$ follows from applying mirror inversion with respect to the xz plane to $J_y = \varepsilon_{yz}(\vec{M})E_z$.

[59] Appendix C discusses the smallness of $\varepsilon_{yz}^2/\varepsilon_{zz}$ from a theoretical point of view. Alternatively, data in [6] [Fig. 1(a), $\theta_F \approx 10^3$ rad/cm] imply using Eq. (13) of [5] $\sigma_{xy} \approx 14\ (\Omega\,\mathrm{cm})^{-1}$. This translates to $\varepsilon_{xy} = 0.05$ (relative) at $\hbar\omega = 2$ eV, hence $\varepsilon_{xy}^2/\varepsilon_{xx} \approx 2 \times 10^{-4}$ (for $\varepsilon_{xx} \approx 13$). This is small compared to $\varepsilon_{xx} - \varepsilon_{zz} = 0.02$ (see Appendix C).

[60] R. R. Birss, *Symmetry and Magnetism* (North-Holland, Amsterdam, 1964).

[61] Š. Višňovský, Czech. J. Phys. B **36**, 1424 (1986).

[62] K. Postava, D. Hrabovsky, J. Pistora, A. R. Fert, S. Visnovsky, and T. Yamaguchi, J. Appl. Phys. **91**, 7293 (2002).

[63] S. Bhagavantam, *Crystal Symmetry and Physical Properties* (Academic, London and New York, 1966).

[64] J. Hamrlová, J. Hamrle, K. Postava, and J. Pištora, Phys. Status Solidi B **250**, 2194 (2013).

[65] E. de Ranieri, A. W. Rushforth, K. Výborný, U. Rana, E. Ahmad, R. P. Campion, C. T. Foxon, B. L. Gallagher, A. C. Irvine, J. Wunderlich *et al.*, New J. Phys. **10**, 065003 (2008).

[66] S. Piano, R. Grein, C. J. Mellor, K. Výborný, R. Campion, M. Wang, M. Eschrig, and B. L. Gallagher, Phys. Rev. B **83**, 081305 (2011).

[67] T. Jungwirth, J. Mašek, K. Y. Wang, K. W. Edmonds, M. Sawicki, M. Polini, J. Sinova, A. H. MacDonald, R. P. Campion, L. X. Zhao *et al.*, Phys. Rev. B **73**, 165205 (2006).

[68] E. M. Hankiewicz, T. Jungwirth, T. Dietl, C. Timm, and J. Sinova, Phys. Rev. B **70**, 245211 (2004).

[69] G. M. Sipahi, R. Enderlein, L. M. R. Scolfaro, and J. R. Leite, Phys. Rev. B **53**, 9930 (1996).

[70] Y. Zhang and S. Das Sarma, Phys. Rev. B **72**, 125303 (2005).

[71] The standard way to microscopically link Γ to potential disorder is to include potential of randomly positioned impurities into $\hat{H}$ and average over the positions. This procedure is explained in Sec. 8.1.2 of G. Mahan, *Many-Particle Physics*, 3rd ed. (Kluwer Academic/Plenum, New York, 2000). Alternatively, $\Gamma/\hbar$ can also be introduced as inverse relaxation time when the electron is weakly interacting with its surroundings [72].

[72] M. Lax, Phys. Rev. **109**, 1921 (1958).

[73] P. Allen, in *Conceptual Foundations of Materials A Standard Model for Ground- and Excited-State Properties*, Contemporary Concepts of Condensed Matter Science Vol. 2, edited by S. G. Louie and M. L. Cohen (Elsevier, Amsterdam, 2006), pp. 165–218.

[74] J. Kolorenč, L. Smrčka, and P. Středa, Phys. Rev. B **66**, 085301 (2002).

[75] B. Al-Qadi, N. Nishizawa, K. Nishibayashi, M. Kaneko, and H. Munekata, Appl. Phys. Lett. **100**, 222410 (2012).